Sensitivity of Mesoscale Gravity Waves to the Baroclinicity of Jet-Front Systems

SHUGUANG WANG AND FUQING ZHANG

Department of Atmospheric Sciences, Texas A&M University, College Station, Texas

(Manuscript received 26 January 2006, in final form 5 June 2006)

ABSTRACT

This study investigates the sensitivity of mesoscale gravity waves to the baroclinicity of the background jet-front systems by simulating different life cycles of baroclinic waves with a high-resolution mesoscale model. Four simulations are made starting from two-dimensional baroclinic jets having different static stability and wind shear in order to obtain baroclinic waves with significantly different growth rates. In all experiments, vertically propagating mesoscale gravity waves are simulated in the exit region of upper-tropospheric jet streaks. A two-dimensional spectral analysis demonstrates that these gravity waves have multiple components with different wave characteristics. The short-scale wave components that are preserved by a high-pass filter with a cutoff wavelength of 200 km have horizontal wavelengths of 85–161 km and intrinsic frequencies of 3–11 times the Coriolis parameter. The medium-scale waves that are preserved by a bandpass filter (with 200- and 600-km cutoff wavelengths) have horizontal wavelengths of 250–350 km and intrinsic frequencies less than 3 times the Coriolis parameter. The intrinsic frequencies of these gravity waves tend to increase with the growth rate of the baroclinic waves; gravity waves with similar frequency are found in the experiments with similar average baroclinic wave growth rate but with significantly different initial tropospheric static stability and tropopause geometry. The residuals of the nonlinear balance equation are used to assess the flow imbalance. In all experiments, the developing background baroclinic waves evolve from an initially balanced state to the strongly unbalanced state especially near the exit region of upper-level jet fronts before mature mesoscale gravity waves are generated. It is found that the growth rate of flow imbalance also correlates well to the growth rate of baroclinic waves and thus correlates to the frequency of gravity waves.

1. Introduction

Gravity waves are one of the most fundamental dynamical processes in the atmosphere. They are closely associated with a wide variety of atmospheric processes ranging from microscale to global-scale dynamical phenomena including but not limited to clear air turbulence, convection, and general circulations. Gravity waves can be generated by shear instability, convection, topography, frontogenesis, geostrophic adjustment, and wave–wave interactions (Koch and Dorian 1988; Fritts and Alexander 2003). They can transfer significant amounts of energy and momentum (e.g., Holton et al. 1995), initiate and organize convection (Zhang et al. 2001, and references therein), and generate and modulate atmospheric turbulence (e.g., Shapiro 1981). Typical mesoscale gravity waves have horizontal wavelengths of 50–500 km, vertical wavelengths of 1–4 km, intrinsic periods of 0.5–4 h, surface amplitudes of 0.5–15 hPa, and phase velocities of 15–35 m s^{-1}. Uccellini and Koch (1987, hereinafter UK87), after a survey of 13 observational case studies, found that mesoscale gravity waves frequently occur in the exit region of upper-level jet streaks and on the cold-air side of surface frontal boundaries. They speculated that the flow imbalance and subsequent geostrophic adjustment near the jet streak are likely responsible for generating these gravity waves. The preferred region of gravity wave activity in UK87 was also later verified in many other observational studies (e.g., Schneider 1990; Ramamurthy et al. 1993; Koch and O'Handley 1997; Bosart et al. 1998; Koppel et al. 2000; Guest et al. 2000; Plougonven and Teitelbaum 2003; Wu and Zhang 2004). The synoptic and mesoscale settings favorable for these gravity wave activities are quite typical for midlatitude jet-front systems accompanied by baroclinic instability (Pierrehumbert and Swanson 1995).

Corresponding author address: Dr. Fuqing Zhang, Department of Atmospheric Sciences, Texas A&M University, College Station, TX 77845-3150.
E-mail: fzhang@tamu.edu

DOI: 10.1175/MWR3314.1

O'Sullivan and Dunkerton (1995) made a first attempt to simulate gravity waves generated from idealized baroclinic waves with a hemispheric, hydrostatic, primitive equation model and investigate wave generation through geostrophic adjustment. Subsynoptic-scale gravity waves with horizontal wavelengths of 600–1000 km in the jet-exit region were produced in their simulations. However, the smallest horizontal grid spacing used in their hemispheric model was approximately 50 km, which is too large to resolve typical mesoscale gravity waves (horizontal wavelengths 50–500 km; e.g., UK87; Zhang and Koch 2000; Zhang et al. 2001; Koch et al. 2001). Recently Zhang (2004, hereafter Z04) performed idealized baroclinic wave simulations using a mesoscale model with horizontal grid spacing as small as 3.3 km in which mesoscale gravity waves with prevalent horizontal wavelengths of 100–200 km and intrinsic frequencies of approximately 3–4 times the Coriolis parameter are generated in the exit region of the upper-level jet-front system. These results are consistent with past observational studies. Balance adjustment, as a generalization of geostrophic adjustment, was hypothesized as the source mechanism for the generation of these gravity waves (Z04).

As an extension of Z04, the current study seeks to understand what factors of the background baroclinic waves determine the gravity wave characteristics. Wind shear and tropospheric static stability, two of the determining factors for baroclinic growth rate and baroclinicity in the two-dimensional Charney model (Lindzen and Farrell 1980), are altered by changing the tropopause geometry and tropospheric potential vorticity in the initial two-dimensional jet of Z04. Because of the extreme complexity, we do not attempt to explore the full parameter space of baroclinic development. Methods and experimental design will be described in the next section. Section 3 will provide an overview of all experiments, followed by detailed comparison of wave characteristics in section 4. Further discussions of flow imbalance and balance adjustment will be presented in section 5. Section 6 will conclude this study with a summary and implications.

2. Initial conditions and experimental design

The fifth-generation National Center for Atmospheric Research–Pennsylvania State University Mesoscale Model (MM5; Dudhia 1993) used in this study is configured to eliminate the effects of spherical geometry, topography, and moist processes. The procedure to create balanced initial conditions for different experiments is the same as in Z04. More specifically, a simplified two-dimensional (2D) potential vorticity (PV) inversion (Davis and Emanuel 1991) is first employed to create a 2D idealized baroclinic jet similar to Simmons and Hoskins (1978). The 2D jet is expanded to three dimensions (3D) assuming zonal homogeneity. The 3D PV distribution, with the addition of a PV perturbation at the tropopause level (Rotunno and Bao 1996), is then inverted by the 3D PV inversion technique (Davis and Emanuel 1991) to produce the initial conditions for the coarse MM5 domain. Top boundaries are set at a constant temperature of 600 K and lateral boundaries are given by zero relative vorticity. All experiments employ three model domains with grid spacing of 90, 30, and 10 km, respectively. The coarse model domain (D1) extends 27 000 km in the east–west direction and 9000 km in the north–south direction. We chose such a huge domain in order to minimize the influence from lateral boundaries. The 30-km domain (D2) is a rectangular subdomain 6300 km long and 4800 km wide within D1. The 10-km domain (D3) is a rectangular subdomain 3100 km long and 2500 km wide within D2.

The growth rate of the fastest-growing normal mode for baroclinic waves in the simple Charney model (Lindzen and Farrell 1980) is given by a baroclinicity index,

$$\sigma = 0.31 \frac{f}{N}\left|\frac{\partial u}{\partial z}\right|, \tag{1}$$

where static stability N^2, the Coriolis parameter f, and the average vertical shear of the zonal wind $|\partial u/\partial z|$ are important for baroclinic instability. In addition to the control simulation (CNTL; exactly the same experiment as in Z04), three more high-resolution experiments are conducted by modifying static stability and wind shear. The geometry of the tropopause and the tropospheric potential vorticity are modified in the first step of the 2D PV inversion. As a result, these modifications change the horizontal and vertical shear and static stability. By tuning these large-scale parameters, the growth rates and the life cycles of the baroclinic waves may be changed.

Sensitivity experiment LowS (LowN) differs from CNTL in that the slope of the initial tropopause (initial tropospheric PV) is changed, leading to a relatively slower (faster) baroclinic growth rate. The tropospheric PV is 0.5 PVU for CNTL and 0.25 PVU for LowN. A flatter tropopause and lower tropospheric PV will lead to stronger vertical shear and lower tropospheric static stability. The other experiment (LowNlowS) changes the initial shape of the tropopause and tropospheric PV simultaneously to obtain baroclinic waves with growth rate similar to the CNTL simulation. The initial 0.46

TABLE 1. Summary of model configurations for the four experiments (listed in the first column). The second column is tropospheric potential vorticity PV_T used in the 2D inversion. The third column is the maximum zonal wind speed. The fourth and fifth columns are start times of domains 2 and 3, respectively. The last column is the total model integration time.

Expt	PV_T (PVU)	U_{max} (m s^{-1})	D2 (h)	D3 (h)	Tot integration time (h)
CNTL	0.5	46.7	72	84	120
LowS	0.5	39.2	108	96	144
LowN	0.25	56.4	30	36	66
LowNlowS	0.46	38.3	60	72	120

PVU tropospheric PV for LowNlowS is slightly smaller than that used in CNTL, and the slope of the tropopause for LowNlowS is the same as LowS but flatter than CNTL. Planetary rotation, another important factor in determining baroclinicity [Eq. (1)], is fixed to be the same as CNTL for all experiments for simplicity.

The parameters used to initiate the four experiments (including CNTL examined in Z04) are summarized in Table 1, and the initial conditions of all four experiments along an unperturbed meridional cross section is shown in Fig. 1 with the maximum zonal wind speed of each experiment listed in Table 1.

3. Overview of simulated baroclinic waves

The life cycle of the baroclinic waves in CNTL starts from the initial 3D PV perturbations seeded at the tropopause level. After 72 h, surface features commonly found in well-developed baroclinic waves include a continuously deepening surface cyclone and anticyclone, strengthening cold and warm fronts, and

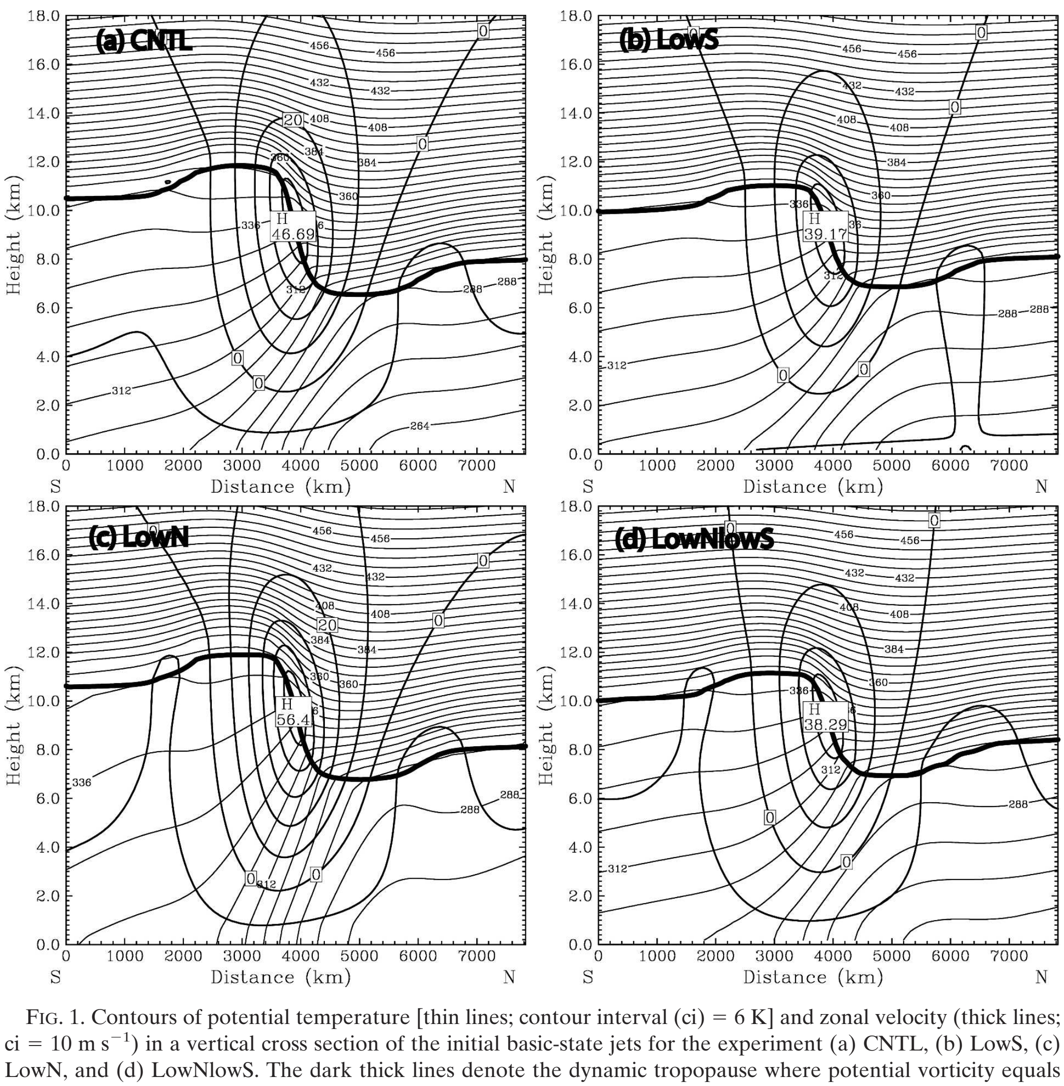

FIG. 1. Contours of potential temperature [thin lines; contour interval (ci) = 6 K] and zonal velocity (thick lines; ci = 10 m s^{-1}) in a vertical cross section of the initial basic-state jets for the experiment (a) CNTL, (b) LowS, (c) LowN, and (d) LowNlowS. The dark thick lines denote the dynamic tropopause where potential vorticity equals 1.5 PVU.

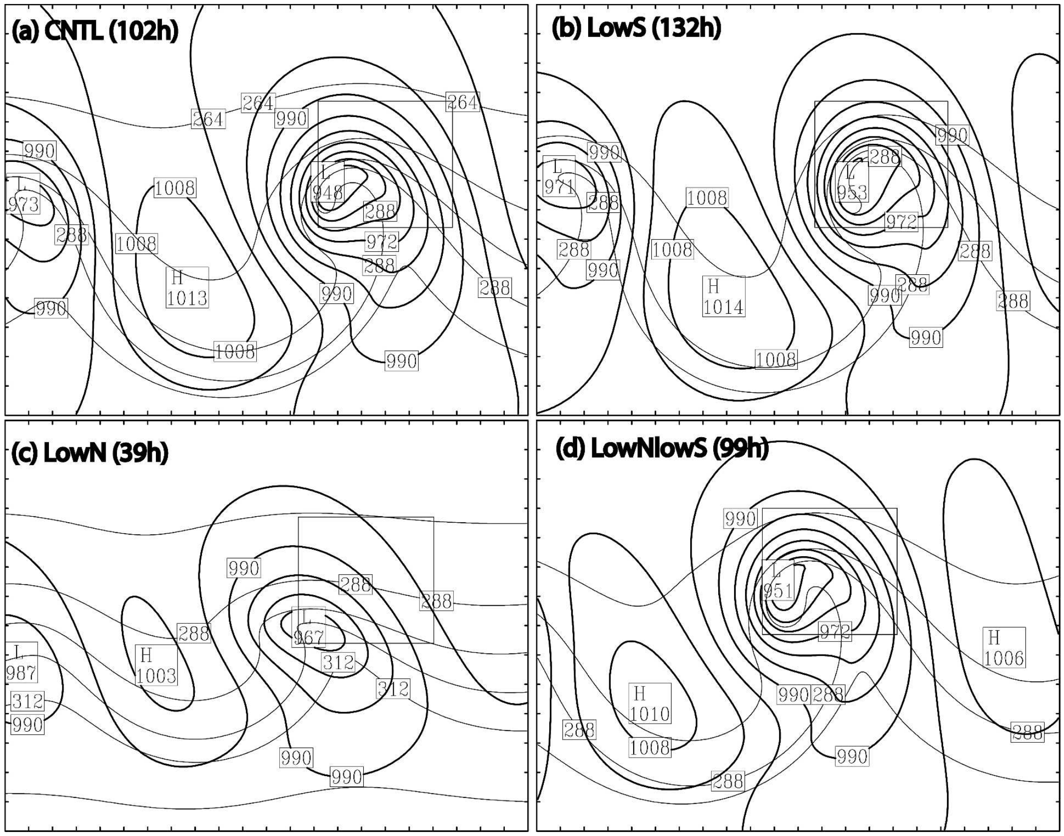

FIG. 2. Surface potential temperature (thin lines; ci = 8 K) and sea level pressure (thick lines; ci = 6 hPa) valid at (a) 102 h for CNTL, (b) 132 h for LowS, (c) 39 h for LowN, and (d) 99 h for LowNlowS plotted on a subset of domain 2. The inner rectangular boxes denote the area plotted in Figs. 7, 9, and 11. The distance between tick marks is 300 km.

emergence of an occluded front as part of a "T-bone" structure (Shapiro and Keyser 1990). The tropopause above the surface cyclone, accompanied by a strengthening upper-level jet steak, descends continuously to the lower troposphere. Around 78 h, an area of imbalance (large residual of the balance equation or ΔNBE) appears near the tropopause level. While the gravity wave signals in the exit region of the upper-level jet streak begin to emerge in the ΔNBE field 24 h later, they are barely noticeable in the vertical velocity fields at this earlier time. At 114 and 120 h, vertical motions show strong signals of gravity waves in the horizontal and vertical planes (Z04).

Despite expected differences in phase, scale, and intensity, typical life cycles of dry baroclinic waves similar to those observed in CNTL have been simulated in all the aforementioned sensitivity experiments. The evolution of the flow from an initially balanced state to a strongly unbalanced state in the vicinity of upper-level jet front and tropopause preceding the mesoscale gravity waves is also qualitatively similar. Figure 2 shows the surface features approximately 9–12 h before mature gravity waves appear in the vertical motion and temperature fields at upper levels when imbalance becomes well developed in all cases (refer to Table 2 for the display time of each case). At this time, the surface cyclones in the four cases are all well developed with minimum sea level pressure (SLP) of 940–965 hPa. In each case warm air has been wrapped into the center of the cyclone to form a warm core, and the surface occluded front has begun to form a T-bone structure.

The horizontal scale of the baroclinic waves, which is close to the Rossby radius of deformation in a stratified atmosphere $\lambda_R = NH/f$, varies slightly among the experiments. In LowN and LowS the horizontal wavelengths are ~3600 km, and they are ~3900 km in CNTL and LowNlowS.

The horizontal wind speeds at 300 hPa, the level of maximum jet strength in the initial conditions, are shown in Fig. 3 at the same times as the corresponding panels in Fig. 2. Both the strength and the shapes of the upper-level jets vary significantly among the experi-

TABLE 2. Summary of the baroclinic wave characteristics for the four experiments. Column 2 lists the times of maximum imbalance when surface and 300 hPa are shown in Figs. 7 and 8. Columns 3 and 4 are the maximum wind speeds at 300 hPa and the minimum SLP, respectively, at these times. Column 5 is the time mature gravity waves (GWs) shown in Fig. 7. Column 6 is minimum SLP at the times listed in column 5. Column 7 is the zonal wavelength of the baroclinic waves (BWs). Columns 8 and 9 list the average growth rate and the period during which the average growth rates are estimated, respectively.

Expt	Times in Fig. 2 (h)	Jet strength (m s^{-1})	Min SLP (hPa)	Mature GWs time (h)	Min SLP (hPa)	Wavelength of BWs (km)	Avg growth rate (h^{-1})	Period to avg (h)
CNTL	102	45.9	948	114	934	3900	0.0129	0–114
LowS	132	39.4	953	144	944	3600	0.0106	0–144
LowN	39	56.2	967	48	948	3600	0.0264	0–48
LowNlowS	99	40.3	951	111	940	3900	0.0124	0–111

ments. For example, the flow in LowN, in the presence of a stronger jet, is relatively flat with less curvature (Fig. 3c). Conversely, the jets downstream of the trough in both LowS and LowNlowS bend northward (Figs. 3b and 3d). Also at the same times at 13 km, strong divergence develops downstream of the trough with weaker signals of gravity waves beginning to emerge in the exit region of the jet streaks (Fig. 4). These weaker wave signals will evolve into coherent mature gravity waves 9 to 12 h later in the 13-km divergence fields (Fig. 5).

The initial tropopause-level PV anomaly develops with a primary cyclone located just below the upper-level PV perturbation, accompanied by secondary cyclogenesis both upstream and downstream. Evolution of the minimum SLP in the major low pressure centers (estimated in domain 2) for all cases is plotted in Fig. 6a. By changing either the slope of the tropopause (LowS) or the tropospheric PV (LowN) in the initial conditions, the SLP decreases slower or faster than that of CNTL (Fig. 6a). The strength of the surface cyclone in LowNlowS, both factors modified simultaneously, is similar to that of CNTL at all times. We also compute

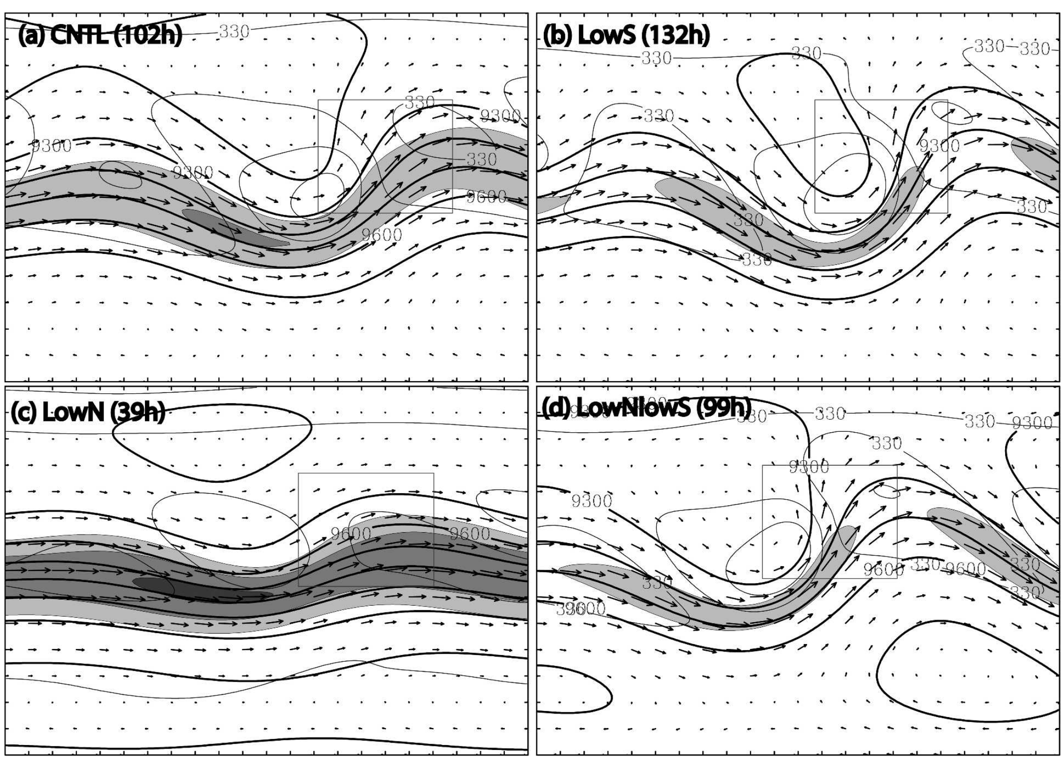

FIG. 3. The 300-hPa wind vectors (magnitude greater than 35 m s^{-1} light shaded, greater than 55 m s^{-1} dark shaded), wind, geopotential heights (thick lines; ci = 100 m), and potential temperature (thin lines; ci = 5 K) valid at (a) 102 h for CNTL, (b) 132 h for LowS, (c) 39 h for LowN, and (d) 99 h for LowNlowS. The distance between tick marks is 300 km.

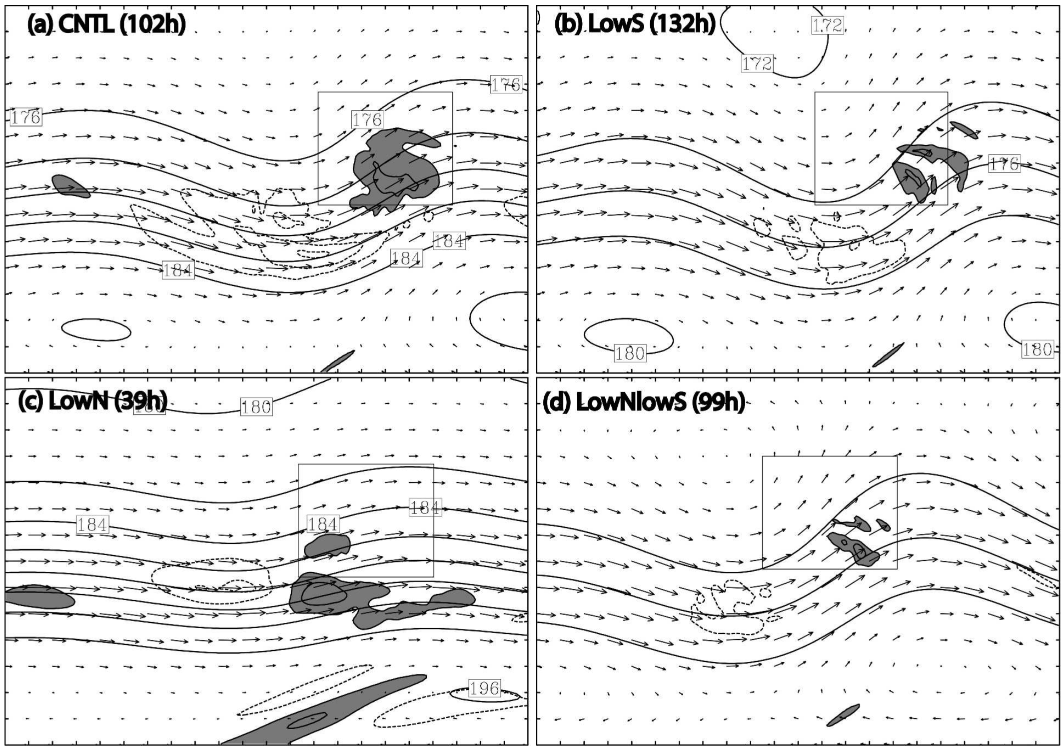

FIG. 4. The 13-km horizontal divergence (thin line; solid and shaded, positive; dashed, negative; ci = 2×10^{-6} s^{-1}), pressure (thick line; ci = 2 hPa), and wind vectors valid at (a) 102 h for CNTL, (b) 132 h for LowS, (c) 39 h for LowN, and (d) 99 h for LowNlowS. The distance between tick marks is 300 km.

the minimum pressure perturbations of the primary surface cyclones (in domain 1 from the initial time) by subtracting zonal-mean SLP from the SLP field. Time series of the maximum pressure perturbations (in absolute value) of the primary cyclones are plotted in Fig. 6b. Similarly, the wind perturbations u', v', and w' are also calculated. The perturbation kinetic energy of the baroclinic waves, defined as the sum of kinetic energy $\{K' = (1/2)[(u')^2 + (v')^2 + (w')^2]\}$ integrated from the whole domain, is shown in Fig. 6c.

Following Badger and Hoskins (2001), we defined an average growth rate of the baroclinic waves in terms of perturbation kinetic energy from time 0 to t as

$$\sigma = \frac{\log(K_t'/K_0')}{t}, \qquad (2)$$

where K_0' and K_t' are the perturbation kinetic energy at time 0 and t, where t is the time when the gravity waves become mature in each experiment (detailed below). Consistent with Fig. 6c, the average growth rate of 0.0129 h^{-1} in CNTL in terms of perturbation kinetic energy is similar to that in LowNlowS (0.0124 h^{-1}), both of which are larger than that in LowS (0.0106 h^{-1}) and smaller than that in LowN (0.0264 h^{-1}).

4. Sensitivity of gravity waves to the baroclinicity

a. *Overview of gravity waves*

Mesoscale gravity waves, similar to those in CNTL, have been generated during the life cycle of each different baroclinic wave. These gravity waves begin to be visible over the strong divergent regions in the exit region of the upper-tropospheric jet streaks and downstream of the upper-level troughs (Fig. 4). These waves evolve into several distinct wave crests and troughs 9–12 h later (Fig. 5). Figure 7 shows a zoomed-in display (box areas in Figs. 2–5) of the mature gravity waves in the vertical velocity and potential temperature fields at 13 km with the corresponding vertical profiles displayed in Fig. 8. The display times are selected based on the presence of two or more crests and troughs in the vertical motion fields. Examinations of the surface and upper-tropospheric features demonstrate a common synoptic pattern for mesoscale gravity waves identified by UK87.

To better detect the gravity waves, we employ a 2D spectral analysis technique (e.g., Lim 1989) applied in the horizontal planes to separate the gravity waves into different wavenumber bands. Three 2D filters

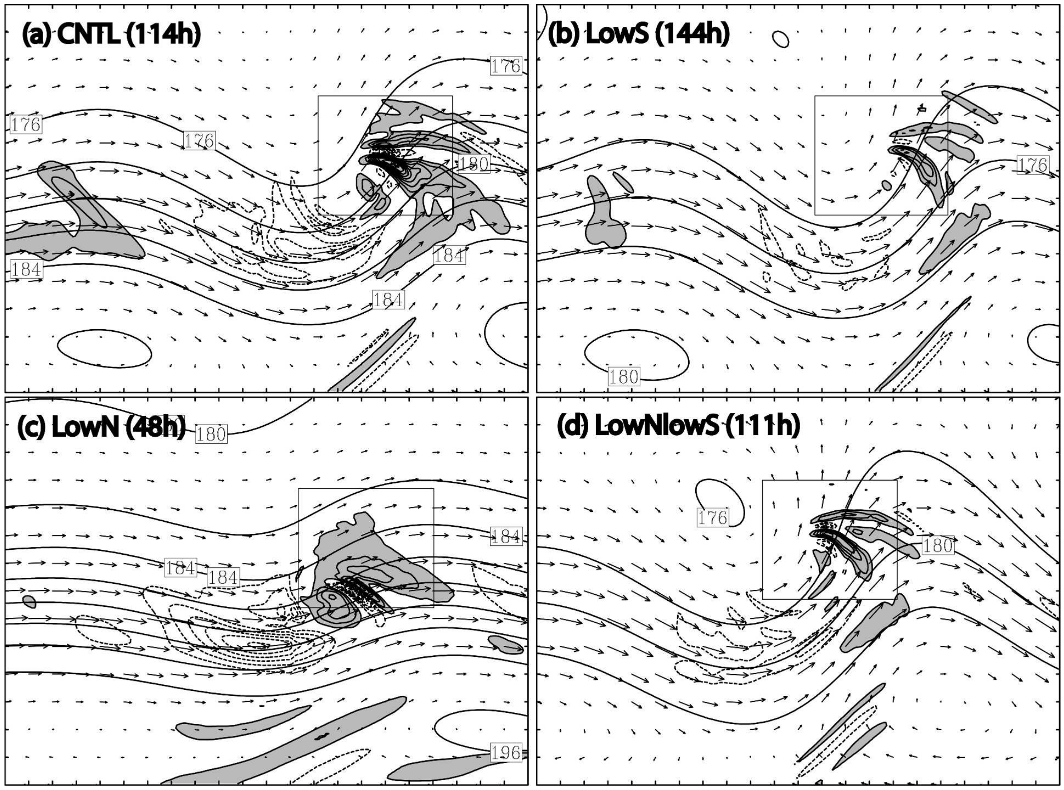

FIG. 5. The 13-km divergence (thin lines; solid and shaded, positive; dashed, negative; ci = 2×10^{-6} s^{-1}), pressure (thick lines; ci = 2 hPa), and wind vectors valid at (a) 114 h for CNTL, (b) 144 h for LowS, (c) 48 h for LowN, and (d) 111 h for LowNlowS. The distance between tick marks is 300 km.

(a 200-km high pass, a 200–600-km bandpass, and a 600-km low pass) are applied to vertical motions at every vertical level. We focus on the same times as those in Figs. 7 and 8 when there are clear signals of mature gravity waves (114 h for CNTL, 144 h for LowS, 48 h for LowN, and 111 h for LowNlowS). The wave signals of vertical velocities preserved by the 200-km high-pass filter, referred to as short-scale waves later on, are shown in Figs. 9 and 10 on the same horizontal planes and cross sections as in Figs. 7 and 8. The gravity wave signals preserved by the 200–600-km bandpass filter, referred to as medium-scale waves later on, are shown in Fig. 11 at 13 km and in the cross sections (Fig. 12) along the center of the wave trains. There are also some weak subsynoptic-scale gravity wave signals after applying the 600-km low-pass filter at 13 km but the vertical motions at these scales are dominated by classical large-scale patterns with strong descent upstream of the trough and ascent downstream (Fig. 13). Although the choice of the cutoff wavelengths is rather subjective, the spectral analysis suggests that a broad spectrum of gravity waves is simulated in each experiment. Also, wave vectors of larger-scale gravity waves have an increasingly larger eastward component in all experiments. Because the subsynoptic-scale gravity wave signals are very weak and often hardly identifiable, we chose not to examine them any further.

The spectral decomposition shows that the medium-scale wave components, which were not evident in Z04 using unfiltered model output (Fig. 7), are comparable in magnitude to the short-scale waves. Moreover, the spectral analysis reveals coherent vertical structures of both short-scale and medium-scale gravity waves in the troposphere (Figs. 10 and 12) that are not obvious in the unfiltered model output (Fig. 8). The vertical wavelengths of both the short-scale and medium-scale gravity waves below the tropopause level are considerably larger than those in the stratosphere (Figs. 10 and 12). The decrease in vertical wavelengths of the gravity waves from the troposphere to the stratosphere may be attributed to the variations of static stability across the tropopause (e.g., Salby and Garcia 1987).

The vertical structures of the filtered wave signals also show apparent connections between the upper-tropospheric/lower-stratospheric jet-exit region gravity waves and the lower-tropospheric waves above the surface fronts, which further suggests that the role of surface frontogenesis in the wave generation cannot be

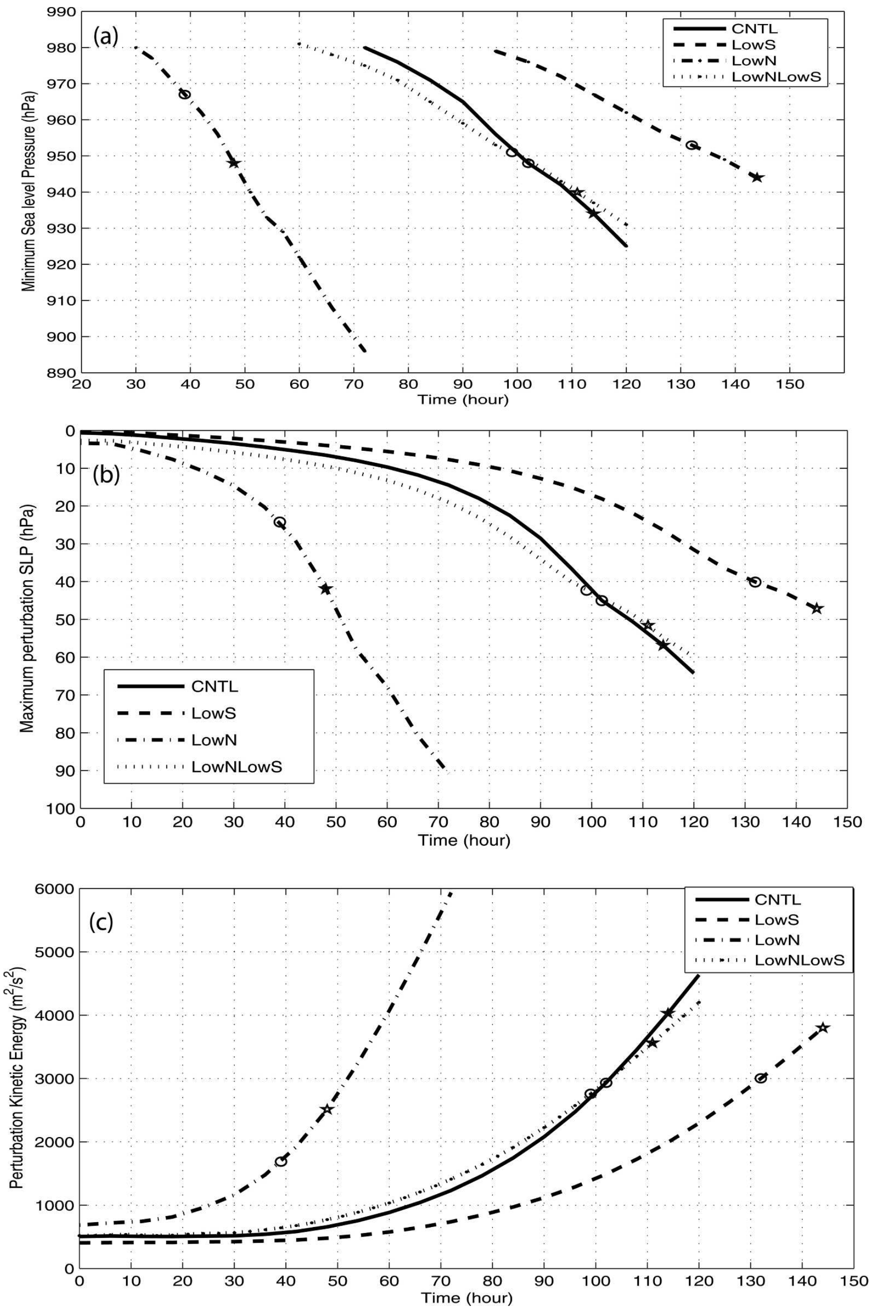

FIG. 6. Time evolution of (a) the minimum SLP (hPa) in domain 2, (b) the absolute value of maximum perturbation SLP (hPa) of the primary cyclones in domain 1, and (c) total perturbation kinetic energy ($m^2\ s^{-2}$). The ellipses indicate the times for each case plotted in Figs. 2–4 and 15–16. The stars indicate the times plotted in Figs. 5 and 7–13.

ruled out. The following analysis will thus examine the characteristics of both the short-scale and medium-scale components of the jet-exit-region gravity waves.

Assuming the wave vectors are perpendicular to the wave phase fronts, we estimate the horizontal and vertical wavelengths in directions perpendicular to the phase fronts by measuring the distance horizontally and vertically between the maximum and minimum perturbations at or near 13 km. The intrinsic frequency of the gravity waves is then derived using the linear hydrostatic dispersion relationship

$$\omega_i^2 = f^2 + \frac{k^2}{m^2}N^2 = f^2 + \frac{\lambda_h^2}{\lambda_z^2}N^2, \tag{3}$$

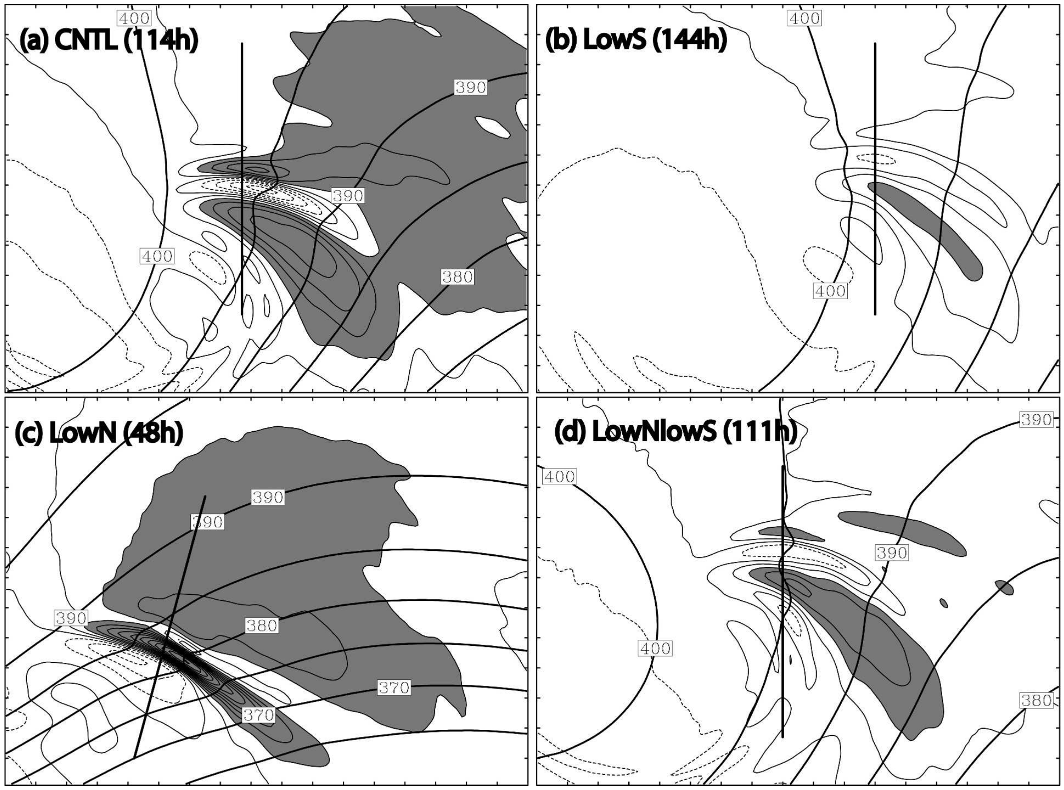

FIG. 7. The 13-km vertical velocity (solid, positive; dashed, negative; ci = 2×10^{-3} m s^{-1}; greater than 5×10^{-3} m s^{-1} shaded) and potential temperature (thick line, ci = 5 K) plotted in domian 3 valid at (a) 114 h for CNTL, (b) 144 h for LowS, (c) 48 h for LowN, and (d) 111 h for LowNlowS. The plotted area is a subset of domain 3 with the locations indicated by the boxes in Fig. 5. The straight lines denote the location of cross sections in Fig. 8. The distance between tick marks is 100 km.

where λ_h (k) and λ_z (m) are the horizontal and vertical wavelength (wavenumber), and N^2 is the static stability in the stratosphere taken as 5×10^{-4} s^{-1} (the value for the unperturbed initial jet configuration). The intrinsic horizontal phase speed is given by $c_i = \omega_i/k$ with negative values for the reason that the upward-propagating gravity waves with downward-propagating phase have negative horizontal and vertical wavenumbers given a positive intrinsic frequency. On the other hand, the intrinsic horizontal phase speed C_{io} can also be estimated (observed) by subtracting the mean wind speed from the mean (ground based) propagation speed C_d of the wave fronts using bandpass-filtered model output averaged over a 6-h period centered on the times shown in Fig. 10.

The intrinsic horizontal phase speeds c_i of short-scale waves in CNTL, LowS, LowN, and LowNlowS derived from the dispersion relationship are −7.4, −8.2, −14.3, and −8.2 m s^{-1}, respectively. These values are consistent with the corresponding observed mean intrinsic phase speeds C_{io} of −8.0, −8.8, −13.9, and −8.2 m s^{-1}, respectively. The intrinsic horizontal phase speeds c_i of short-scale waves are larger than those of medium-scale waves in all cases. The c_i of the medium-scale waves in CNTL, LowS, LowN, and LowNlowS are −13.3, −11.6, −15.0, and −13.2 m s^{-1}, respectively. They are also close to the corresponding C_{io} of −13.8, −11.1, −16.3, and −13.9 m s^{-1}, respectively. The general agreement between c_i derived from Eq. (3) and C_{io} derived from model output at multiple times indicates the filtered gravity waves at this level approximately follow a linear dispersion relationship. Table 3 summarizes the wavelengths (λ_h and λ_z) with their standard deviation error, intrinsic horizontal phase speeds derived from the dispersion relationship (c_i), mean wind speeds, observed ground based phase speeds C_d, and observed intrinsic phase speeds C_{io}.

Despite having a smaller intrinsic phase speed in each experiment, the intrinsic frequency of short-scale waves is always larger than that of corresponding medium-scale waves (Table 3). Among all experiments, the short-scale waves in LowN have the smallest horizontal wavelength (85 km) but the largest vertical wavelength (4 km), corresponding to the highest intrin-

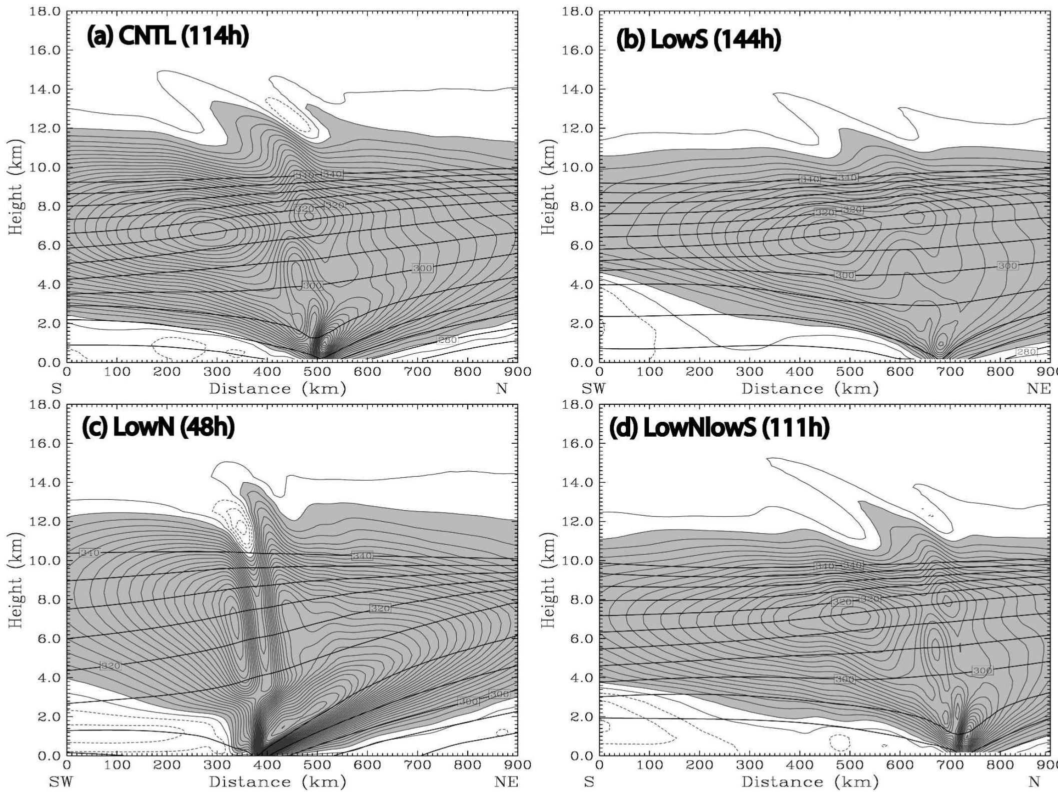

FIG. 8. Vertical velocity (solid, positive; dashed, negative; ci = 5×10^{-3} m s^{-1}; values $> 5 \times 10^{-3}$ shaded) and potential temperature (thick lines, ci = 5 K, >340 K suppressed) along the cross sections indicated by the straight lines denoted in Fig. 7 valid at (a) 114 h for CNTL, (b) 144 h for LowS, (c) 48 h for LowN, and (d) 111 h for LowNlowS.

sic frequency (11f, where f is the Coriolis parameter 0.0001 rad s^{-1}). The medium-scale waves in LowN also have the highest intrinsic frequency (3.2f) and largest vertical wavelength (4 km), but the horizontal wavelength for the medium-scale waves is fairly similar for all experiments. Experiment LowS has the lowest intrinsic frequency for both the short-scale and medium-scale waves among all experiments. The detailed characteristics of the gravity waves in each experiment and their sensitivity to baroclinicity (in comparison with CNTL) will be discussed in the following subsection.

b. Sensitivity to baroclinicity

1) SENSITIVITY TO THE SLOPE OF THE INITIAL TROPOPAUSE

Experiment LowS employs a flatter initial tropopause that results in a weaker jet streak and thus weaker vertical wind shear (Figs. 1a,b). The maximum wind speed for the initial unperturbed 2D jet for LowS is ~39 m s^{-1} and is much weaker than that in CNTL (~47 m s^{-1}). As expected, the average growth rate of the baroclinic waves in LowS (0.0106 h^{-1}) is considerably smaller than that in CNTL (0.0129 h^{-1}). Despite similarity in the minimum SLP of the primary cyclones at 132 h for LowS and 102 h for CNTL (Figs. 2a,b), the flow at the jet stream level shows less curvature for LowS than for CNTL and the difference between the wind speed maximum in LowS and that in CNTL persists even after the baroclinic waves are well developed (Figs. 3a,b).

With the different initial geometry of the tropopause and subsequently different growth rate of the baroclinic waves (Figs. 9a,b; Table 3), the characteristics of the mesoscale gravity waves in the exit region of the upper-level jet streak also differ significantly from CNTL. The short-scale waves in LowS that are preserved by the high-pass filter have a larger horizontal wavelength (~161 km) and lower intrinsic frequency (3.2f) than those of CNTL (wavelength ~128 km and frequency 3.6f). The medium-scale waves in LowS also have an intrinsic frequency of 2.4f, which is less than that in CNTL (2.8f), but the horizontal wavelengths in both experiments are nearly the same (~300 km) (Figs. 11a,b; Table 3).

We also conducted another experiment with a

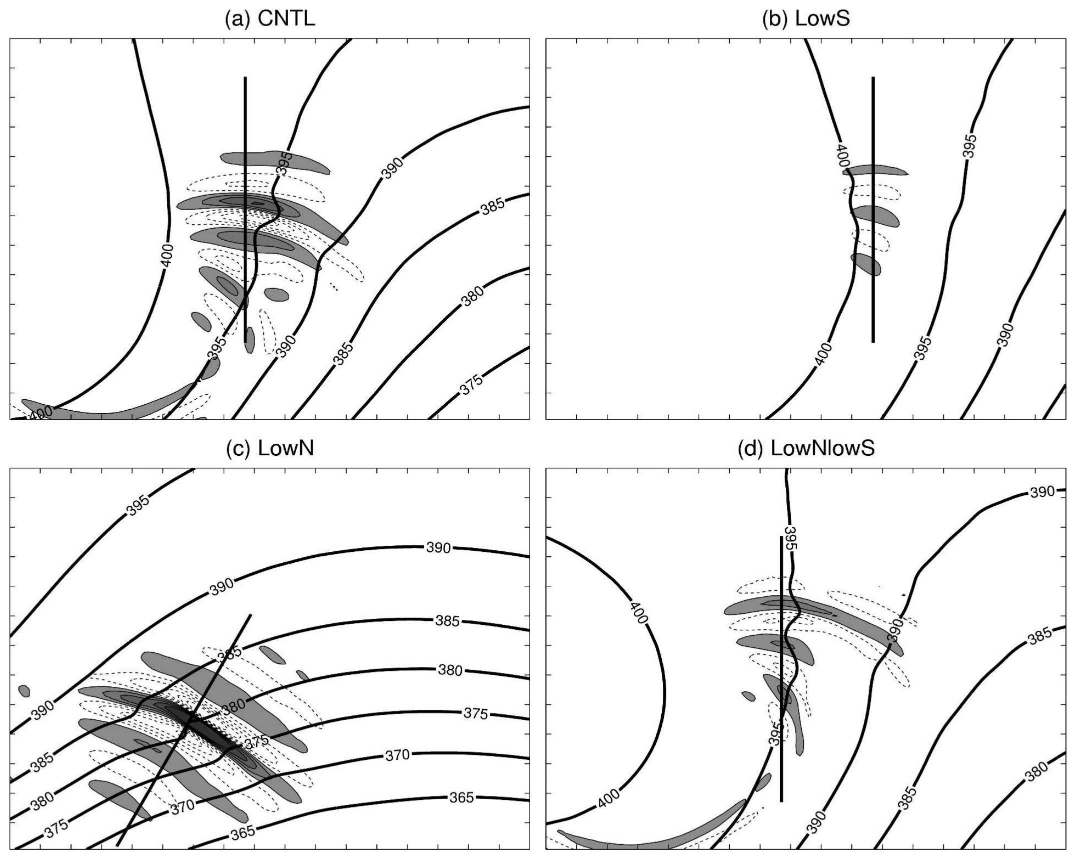

FIG. 9. The 13-km vertical velocity (solid, positive; dashed, negative; ci = 2×10^{-3} m s^{-1}; values $> 1 \times 10^{-3}$ m s^{-1} shaded) filtered by a high-pass filter with cutoff wavelength 200 km and unfiltered potential temperature (thick line; ci = 5 K) valid at (a) 114 h for CNTL, (b) 144 h for LowS, (c) 48 h for LowN, and (d) 111 h for LowNlowS. The straight lines denote the location of the cross sections in Fig. 10. The distance between tick marks is 100 km.

steeper initial tropopause that results in a stronger jet streak and faster baroclinic growth. The gravity waves generated in this experiment (with stronger baroclinicity) have a larger intrinsic frequency than that in CNTL and LowS (not shown). These experiments show that the characteristics of the jet-exit-region gravity waves are closely related to the strength of the initial basic-state jet (the slope of the initial tropopause) and the subsequent difference in baroclinicity of the baroclinic jet-front systems.

2) SENSITIVITY TO TROPOSPHERIC STATIC STABILITY

Experiment LowN reduced the initial tropospheric PV and thus static stability in CNTL by half (Fig. 1d), which leads to a much stronger jet streak (56 m s^{-1}) and thus stronger vertical shear than CNTL at the initial time. The baroclinic wave in LowN, with a stronger vertical shear and a lower tropospheric satiability, grows 1.5 times faster than in CNTL (Fig. 7a). This is qualitatively consistent with the baroclinic index in Eq. (1). The minimum SLP of the primary surface cyclone reaches 967 hPa at 39 h in LowN while the surface low did not reach a similar amplitude until ~102 h in CNTL. The short-scale gravity waves have a much shorter horizontal wavelength (~85 km) and a much higher frequency ($11.0f$) in LowN than in CNTL (128 km, $3.6f$). The medium-scale gravity waves also have a higher intrinsic frequency ($3.2f$) in LowN than that in CNTL ($2.8f$) though their horizontal wavelength is similar. Both experiments LowN and LowS (and their comparison with CNTL) suggest that the larger the growth rate of baroclinic waves, the higher the intrinsic frequency of jet-exit-region mesoscale gravity waves.

3) EXPERIMENT WITH SIMILAR BAROCLINIC GROWTH RATE

Decreasing initial wind shear has an opposite effect on the growth rate of baroclinic waves compared with decreasing tropospheric static stability, as discussed in

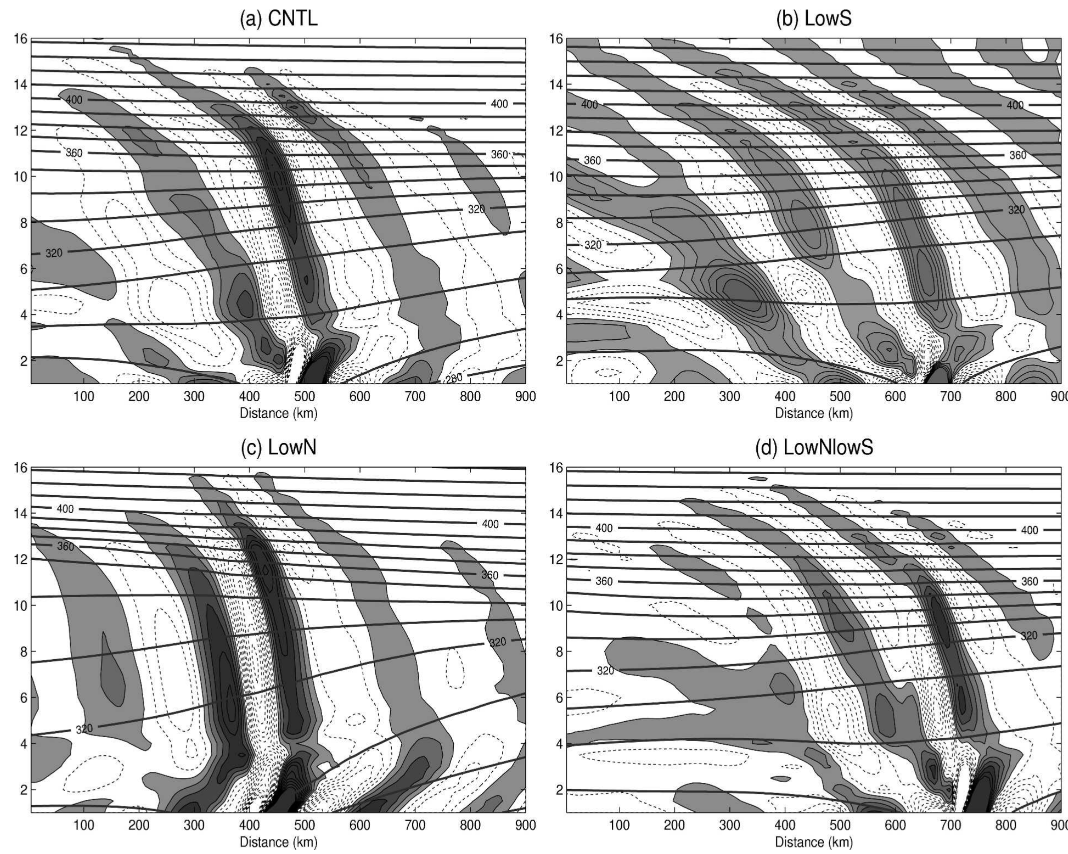

FIG. 10. Filtered vertical velocity (solid, positive; dashed, negative; ci = 2×10^{-3} m s^{-1}; values $> 1 \times 10^{-3}$ m s^{-1} shaded) using a high-pass filter with cutoff wavelength 200 km and unfiltered potential temperature (thick lines; ci = 5 K) along vertical cross sections indicated in Fig. 9 valid at (a) 114 h for CNTL, (b) 144 h for LowS, (c) 48 h for LowN, and (d) 111 h for LowNlowS.

the two experiments LowN and LowS. The experiment LowNlowS has a lower tropospheric stability and a flatter initial tropopause (Fig. 1d; Table 1). The average growth rate of baroclinic waves in this experiment is 0.0124 h^{-1} and is purposely designed to match that in CNTL (0.0129 h^{-1}). As seen in Fig. 6, the minimum SLP of the primary surface cyclone and the magnitude of the perturbation kinetic energy closely follow those of CNTL throughout the 120-h simulation. Weak gravity waves begin to appear in the exit region of the upper-level jet streak at 99 h (Fig. 4d), and they become mature at 111 h (slightly earlier than in CNTL).

The timing of gravity waves' occurrences in LowNlowS is very similar to those in CNTL. We further compare their wave characteristics. Despite having slightly larger horizontal and vertical wavelengths, the short-scale gravity waves in LowSLowN have a similar intrinsic frequency ($3.5f$) to those in CNTL ($3.6f$). The filtered medium-scale waves also have an intrinsic frequency ($2.9f$) similar to those of CNTL ($2.8f$). Considering the similarity found in growth rates of baroclinic waves and wave characteristics of gravity waves between CNTL and LowNlowS, the sensitivity experiment LowNlowS suggests that, at least under the assumption of a constant Coriolis parameter, mesoscale gravity waves generated in the exit region of the upper-level jet-front system may have similar intrinsic frequencies in experiments with similar baroclinic growth rates.

5. Flow imbalance and balance adjustment

a. Overview of flow imbalance diagnosis

At the mature stage of baroclinic waves, the flow may become increasingly unbalanced where jets are distorted and nonlinear effects become important (O'Sullivan and Dunkerton 1995; Hakim 2000). The nonlinear balance equation (Charney 1955) has been used in a number of studies to examine the flow balance beyond geostrophy. For example, Raymond (1992) demonstrated the effectiveness of nonlinear balance for mesoscale processes for a Rossby number around

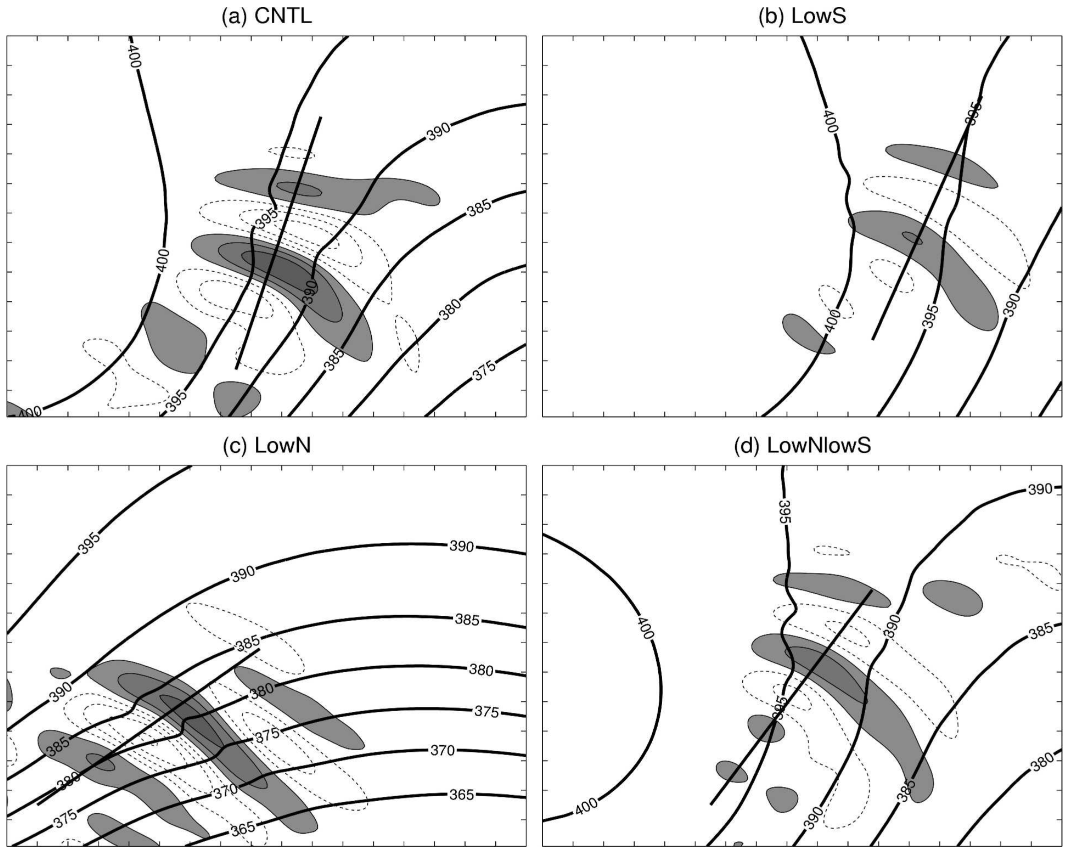

FIG. 11. Same as in Fig. 9 but using a bandpass filter with the cutoff wavelengths 200 and 600 km. The straight lines denote the location of the cross sections in Fig. 12. The distance between tick marks is 100 km.

unity. The residual of the nonlinear balance equation $\Delta\text{NBE} = 2J(\text{u}, \upsilon) + f\zeta - \alpha\nabla^2 P$ has been shown to be more accurate than other imbalance diagnosis devices surveyed in Zhang et al. (2000). Using the ΔNBE diagnosis, Z04 illustrated that flow imbalance can be excited continuously by the distorted jet streaks while the gravity waves are generated. The emission of gravity waves, as an attempt to restore balance, is counteracted by the production of imbalance by the developing baroclinic waves. This transient process, called "balance adjustment" as a generalization of geostrophic adjustment, was hypothesized as the generation mechanism for the jet-exit-region mesoscale gravity waves in Z04.

Figure 14 shows the 6-km dynamic tropopause (PV = 1.5 PVU), vertical velocity, and ΔNBE, illustrating the mesoscale environments for flow imbalance in CNTL as discussed in Z04. The gradually increasing angle between potential temperature and pressure contours indicates the amplifying baroclinic wave (not shown). At 96 h, warm air from the stratosphere begins to intrude downward and forms a temperature ridge and an intense thermal gradient. Regions of downward motions expand downstream from 96 to 108 h. Upon the border areas connecting regions of the strongest upward and downward motions, the magnitude of imbalance (positive ΔNBE region) is continuously enhanced from 90 to 108 h. The strongest imbalance again collocates with the increasing potential temperature gradient downstream of the pressure trough. Regions of the maximum ΔNBE also coincide with the maximum gradient of horizontal divergence with the maximum flow convergence upstream and divergence downstream (not shown).

From a Lagrangian perspective, the dramatic change of vertical motions and horizontal divergence over the discussed area can also be understood by examining the divergence tendency following an air parcel near the tropopause. As a jet streak approaches an upper-level ridge, air parcels experience a significant imbalanced period characterized by dramatic increase in divergence. A full divergence equation in pressure coordinate is given by

$$\frac{dD}{dt} = -D^2 - \nabla\omega \cdot \frac{\partial \mathbf{V}}{\partial P} + 2J(u, \upsilon) + f \cdot \zeta - \nabla^2\Phi, \qquad (4)$$

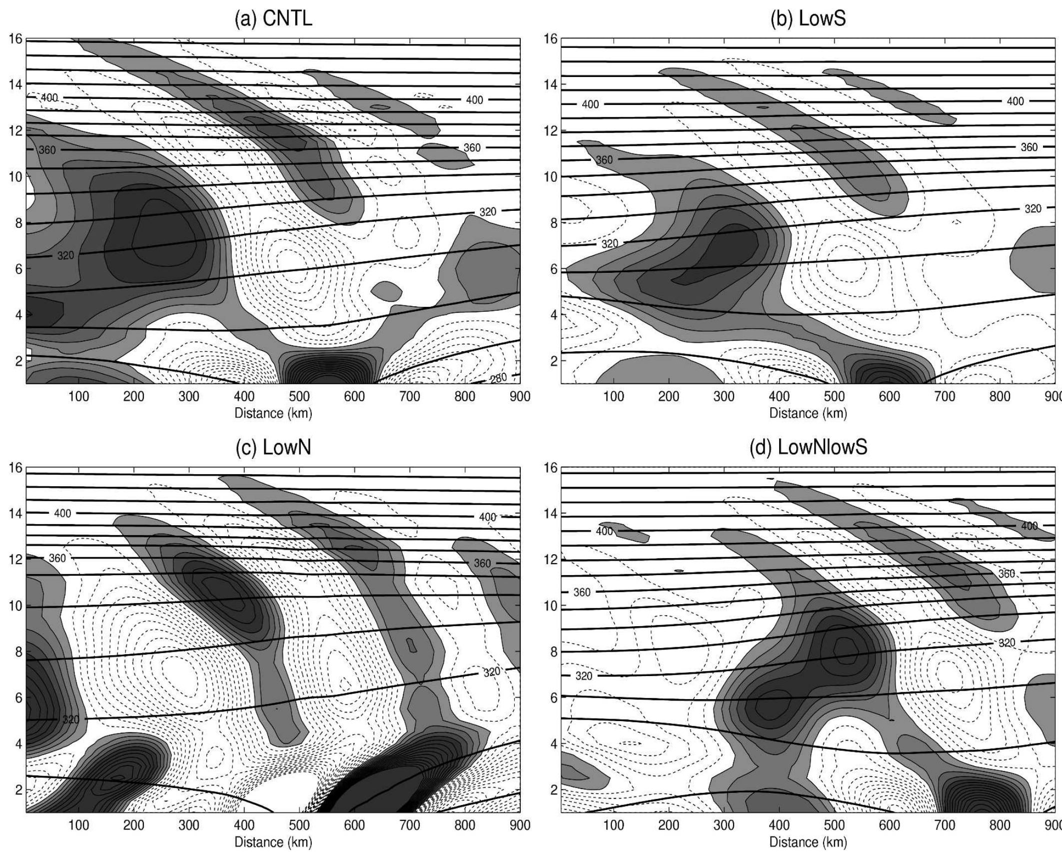

FIG. 12. Same as in Fig. 10 but using a bandpass filter with the cutoff wavelengths of 200 and 600 km and plotting along the cross sections denoted by the straight lines in Fig. 11.

where D, ω, ζ, Φ, and $J(u, v)$ are horizontal divergence, vertical motions, relative vorticity, geopotential height, and Jacobian of horizontal wind components u and v, respectively. The last three terms, which compose ΔNBE, are much larger than all of the other terms in Eq. (4). As discussed by Rotunno et al. (1994), the warm air parcels ride down isentropes from the stratosphere forming the ridge of isotherms at 6 km. Imbalance among the last three terms forces a large increase in divergence as air parcels with lower PV ride up from the troposphere and move through the jet-exit regions. These cross-tropopause motions shape the intense gradient of vertical motions, which are collocated with imbalance regions after 96 h in Fig. 14. The occurrence of ΔNBE in regions with large gradients of vertical motions and in thermal ridges suggest that flow imbalance ΔNBE is closely related to the frontogenesis in the upper troposphere.

The growing localized flow imbalance indicated by an expanding area of positive ΔNBE at 7 km for all experiments is shown in the horizontal planes (Fig. 15) and vertical cross sections (Fig. 16) at 9–12 h before the leading mature gravity waves seen in the level of 13 km (Fig. 7). In all the sensitivity experiments the evolution of ΔNBE from an initially balanced state to the strongly unbalanced state shown in Figs. 15 and 16 is very similar to that of CNTL (refer to Figs. 10 and 11 of Z04). More specifically, Fig. 16 demonstrates that flow imbalance maximizes immediately above the tropopause (around 7 km for most experiments). As discussed for CNTL in Fig. 14, regions of positive ΔNBE at 7 km collocate with a thermal ridge due to the downward intrusion of warm air that originated from the stratosphere (Fig. 15). Also at this time in all experiments, weak gravity wave signals, in the form of alternating positive and negative ΔNBE (Figs. 16a,b,d) and horizontal divergence (Fig. 4), appear immediately downstream of the localized imbalance maxima near the tropopause and upper-level jet-front systems.

b. *Sensitivity of flow imbalance to baroclinic growth rate*

To track the intensity of the imbalance, we construct the time series of averaged imbalance at the 10 points with the largest ΔNBE (Fig. 17) for all the experiments.

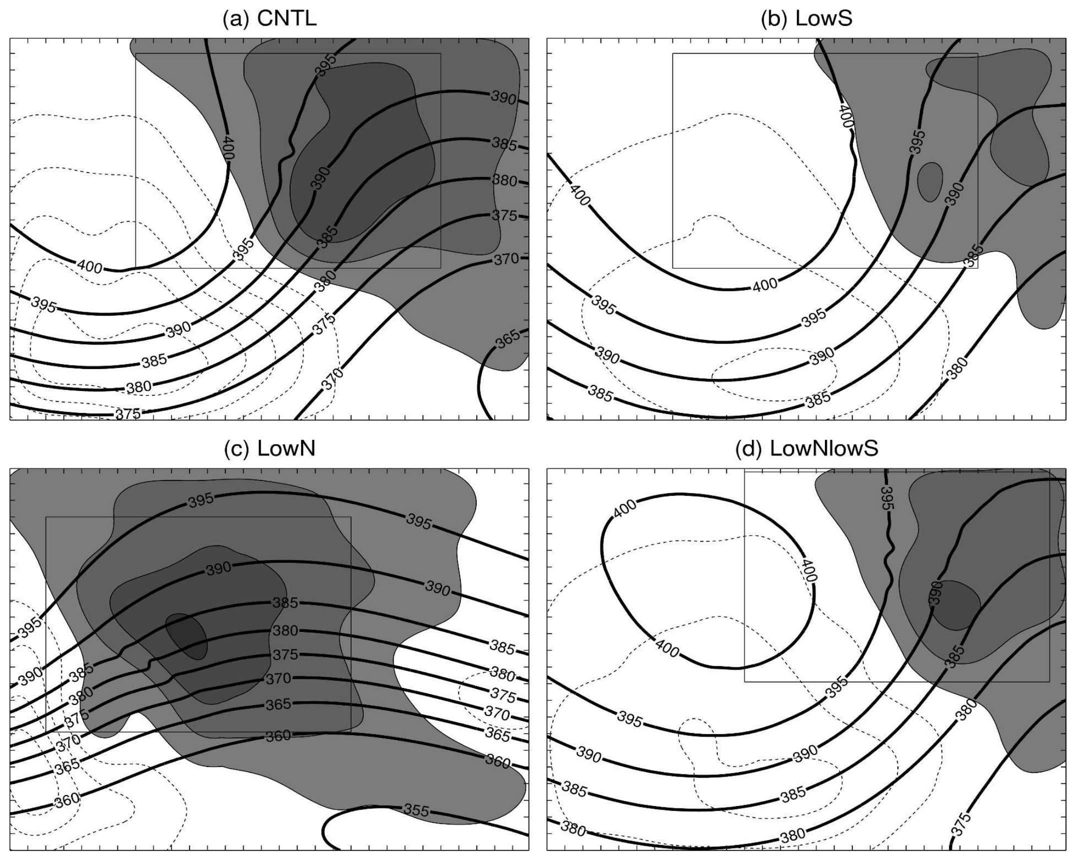

FIG. 13. Same as in Fig. 9 but using a low-pass filter with the cutoff wavelength 600 km displayed on a larger subset of domain 3. The boxes denote the area plotted in Figs. 9 and 11.

TABLE 3. Summary of the gravity wave characteristics for the four experiments. Row 2 shows the times when gravity waves (GWs) are shown in Fig. 7. Rows 3–9 ("short wave" rows) are horizontal wavelengths with standard error, vertical wavelengths with standard error, intrinsic frequency, phase speeds c_i derived from dispersion relation, mean wind speeds along wave vectors, ground-based phase speeds C_d of GWs, and mean flow relative phase speeds C_{io} based on columns 7 and 8 for short-scale GWs in Figs. 9 and 10. The "medium wave" rows are horizontal wavelengths, vertical wavelengths, intrinsic frequency, phase speeds c_i derived from dispersion relation, mean wind speeds along wave vectors, ground-based phase speeds C_d of GWs, and mean flow relative phase speeds C_{io} for medium-scale GWs in Figs. 11 and 12. The last row is the growth rate of ΔNBE calculated from Fig. 17. Note generally C_{io} and c_i agree quite well.

Expt		CNTL	LowS	LowN	LowNlowS
Mature GWs time (h)		114	144	48	111
Short waves	λ_h (km)	128 (±4.3)	161 (±5.7)	85 (±4.0)	145 (±6.2)
	λ_z (km)	2.0 (±0.16)	2.2 (±0.06)	4.0 (±0.06)	2.2 (±0.02)
	ω (10^{-4} rad s^{-1})	3.6	3.2	11.0	3.5
	c_i (m s^{-1})	−7.4	−8.2	−14.3	−8.2
	Wind (m s^{-1})	12	8	21	9
	C_d (m s^{-1})	4	−0.8	7.1	0.8
	C_{io} (m s^{-1})	−8.0	−8.8	−13.9	−8.2
Medium waves	λ_h (km)	300 (±10.3)	300 (±9.5)	300 (±11.3)	280 (±8.9)
	λ_z (km)	3.5	3.0	4.0	3.5
	ω (10^{-4} rad s^{-1})	2.8 (±0.26)	2.4 (±0.19)	3.2 (±0.3)	2.9 (±0.22)
	c_i (m s^{-1})	−13.3	−11.6	−15.0	−13.2
	Wind (m s^{-1})	14	11	27	14
	C_d (m s^{-1})	0.2	−0.1	10.7	0.1
	C_{io} (m s^{-1})	−13.8	−11.1	−16.3	−13.9
Growth rate of the ΔNBE max (h^{-1})		0.061	0.052	0.12	0.057

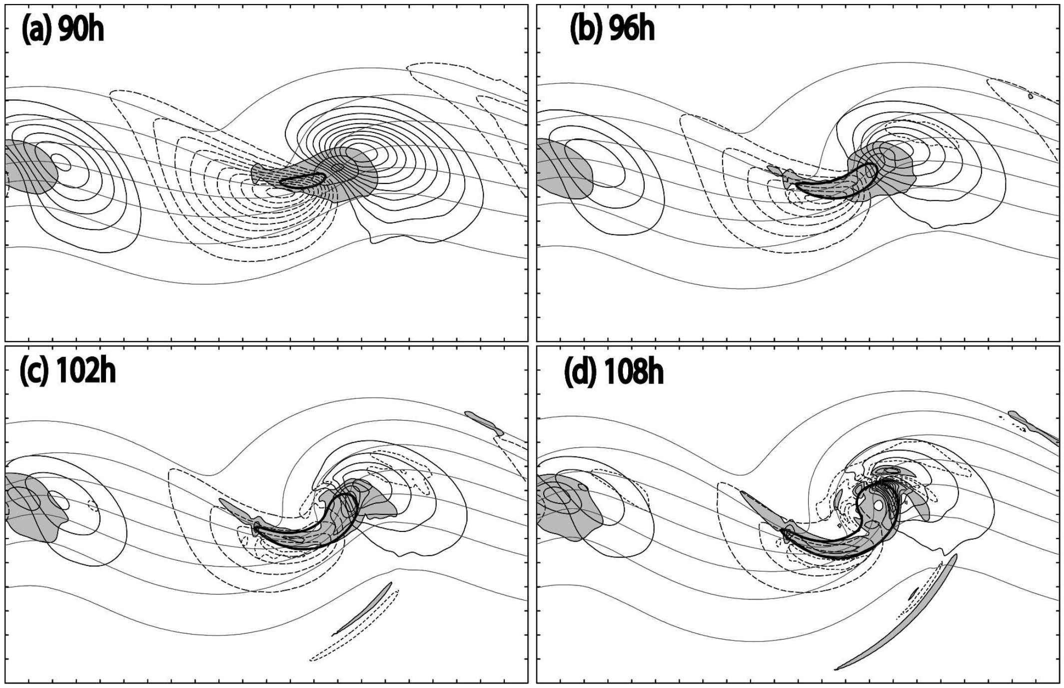

FIG. 14. CNTL-simulated imbalanced flow at 6 km in domain 2 valid at (a) 90, (b) 96, (c) 102, and (d) 108 h; ΔNBE (shaded, solid, positive; dashed, negative; ci = 0.01×10^{-9} s^{-2}), potential temperature (solid lines; ci = 5 K), and vertical velocity [thin lines, solid, positive; dashed, negative; ci = 0.5 cm s^{-1} in (a), 1.0 cm s^{-1} in (b), 1.5 cm s^{-1} in (c), and cm s^{-1} in (d)]. The dark thick lines denote the dynamic tropopause where potential vorticity equals 1.5 PVU. The distance between tick marks is 300 km.

The growth rate of the ΔNBE maximum is calculated from Fig. 17 and summarized in Table 3. The temporal evolutions of the ΔNBE maximum (Fig. 17) suggest that a slower developing baroclinic wave leads to slower and weaker imbalance growth in LowS than that in CNTL. The fastest and strongest growth of imbalance occurs in LowN, which also has the fastest baroclinic growth. Experiments LowSlowN and CNTL, which have similar baroclinic growth rates, have a similar evolution of flow imbalance.

Because the growth of imbalance correlates to the growth rate of the baroclinic waves, and the growth rate of baroclinic waves correlates to the intrinsic frequency of the jet-exit-region gravity waves, the gravity wave frequency is also positively correlated with the growth of flow imbalance. The gravity waves generated in the exit region of the upper-level jet streaks have a higher intrinsic frequency in experiments with a faster growing imbalance. However, the exact relationship between the growing imbalance and the gravity wave frequency cannot be clearly identified in the current study. It also remains unclear what selects the horizontal and vertical scales of gravity waves. This problem can be partly attributed to the complexity of background environments. In addition, strong imbalance also appears near surface fronts (Fig. 16). The roles of surface fronts in the wave generation are also hard to assess since they are an inseparable part of the baroclinic jet-front systems.

6. Summary and discussion

The characteristics of mesoscale gravity waves simulated near the exit region of the upper level jet-front systems during the life cycle of baroclinic waves are addressed numerically in this study. Four different life cycles of idealized baroclinic waves are simulated using a multiply nested mesoscale model (MM5) with grid spacing of 90, 30, and 10 km. The initial baroclinicity of the background environment is modified as a result of using different tropospheric static stability and tropopause geometry for the initial two-dimensional baroclinic jet. Consequently, the growth rate of the baroclinic waves differs significantly among these four experiments. Decreasing the initial slope of the tropopause leads to a weaker jet streak and vertical shear and subsequently results in slower growing baroclinic waves. Decreasing the initial tropospheric PV leads to stronger tropospheric static stability and stronger shear. The subsequent baroclinic waves have a faster growth rate. Similar growth rate of the baroclinic waves is

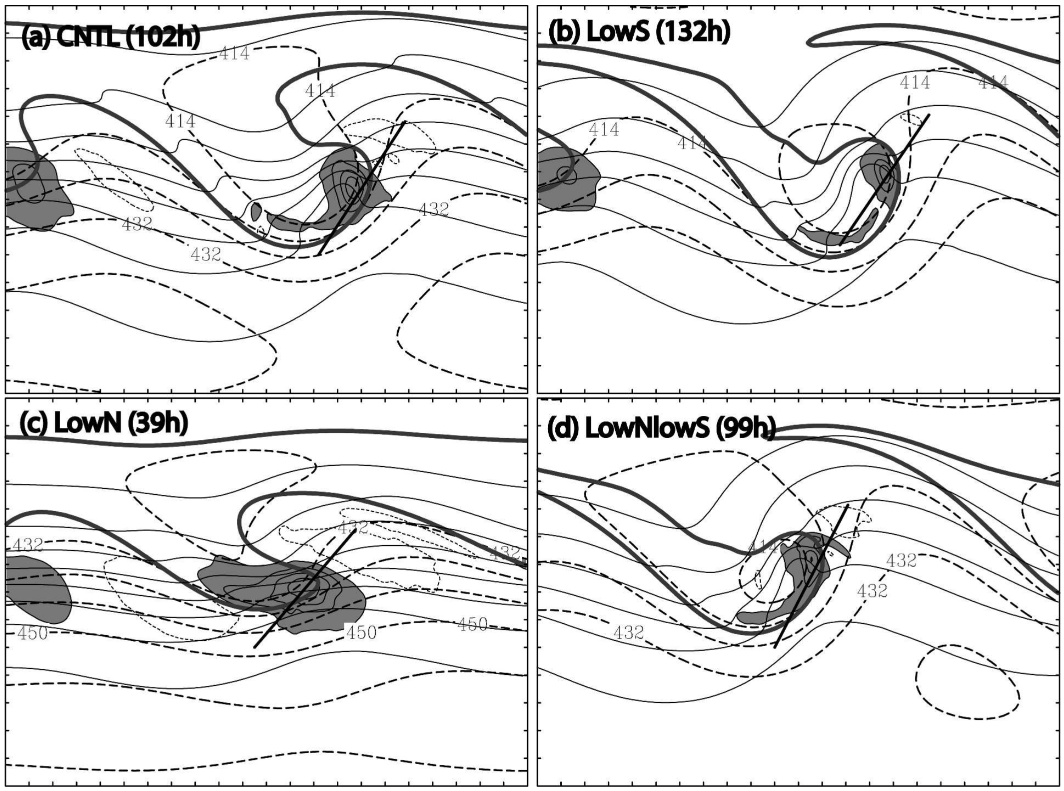

FIG. 15. The 7-km ΔNBE (shaded, solid, positive; dashed, negative; ci = 0.01×10^{-8} s^{-2}), pressure (long-dashed lines; ci = 6 hPa), and potential temperature (thin lines; ci = 5 K) in domain 2 valid at (a) 102 h for CNTL, (b) 132 h for LowS, (c) 39 h for LowN, and (d) 99 h for LowNlowS. The gray thick lines denote the dynamic tropopause where potential vorticity equals 1.5 PVU. The straight lines denote the location of the cross sections in Fig. 16. The distance between tick marks is 300 km.

found in experiments with similar initial baroclinicity but with significantly different initial tropospheric static stability and tropopause geometry.

In all experiments, vertically propagating mesoscale gravity waves are simulated in the exit regions of upper-tropospheric jet streaks near tropopause levels. The synoptic environments of gravity waves consist of surface fronts, upper-level jet fronts, and an upper-level trough, and are consistent with previous studies of typical mesoscale gravity waves synthesized by UK87.

A two-dimensional spectral decomposition technique is applied to better identify the gravity waves in the simulations. The short-scale waves, preserved after applying a high-pass filter with 200-km cutoff wavelength, have horizontal wavelengths of 85–161 km and intrinsic frequencies of 3–9 times the Coriolis parameter. The medium-scale waves that are preserved by a bandpass filter (with 200- and 600-km cutoff wavelengths) have horizontal wavelengths of 250–350 km and intrinsic frequencies below 3 times the Coriolis parameter. Sensitivity tests to the growth rate of baroclinic waves reveal that the intrinsic frequency of these gravity waves tends to increase with the growth rate of the baroclinic waves. The faster the growth rate of the baroclinic waves, the higher the intrinsic frequency of the gravity waves. The intrinsic frequency is similar in experiments with similar baroclinic growth rates.

The jet-exit region mesoscale gravity waves in all experiments are closely related to the localized flow imbalance, which is defined as the residual of the nonlinear balance equation. It is shown that this localized imbalance maximizes at a thermal ridge downstream of the trough collocated with the maximum gradient of horizontal divergence and vertical motions near the upper-level jet-front systems. Time series of the maximum ΔNBE show that imbalance continuously increases while the gravity waves have been generated. Diagnosis of flow imbalance in the four experiments shows that the growth rate of the imbalance is directly correlated to the growth rate of baroclinic waves and thus to the frequency of jet-exit-region gravity waves. In experi-

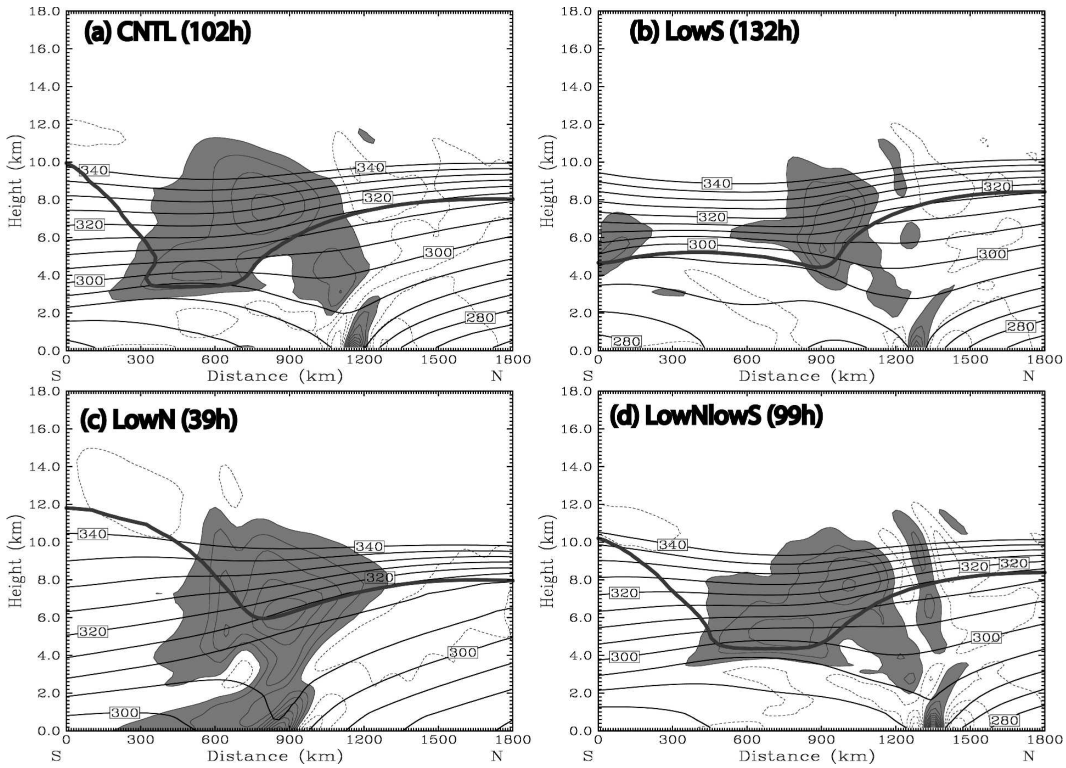

FIG. 16. ΔNBE (shaded, solid, positive; dashed, negative; ci = 0.01×10^{-8} s^{-2}) and potential temperature (ci = 5 K, >340 K suppressed) along the cross sections indicated by the straight lines in Fig. 15 valid at (a) 102 h for CNTL, (b) 132 h for LowS, (c) 39 h for LowN, and (d) 99 h for LowNlowS. The dark thick lines denote the dynamic tropopause where potential vorticity equals 1.5 PVU.

ments with faster growing imbalance, the gravity waves have higher frequency.

This study presents our first attempt to examine the relation between mesoscale gravity waves, the flow imbalance, and the baroclinicity of large-scale jet-front systems using idealized initial conditions and constant Coriolis parameter. We have made no attempt to explore the full parameter space of baroclinic waves because of their complexity. For example, horizontal wind shears can influence the development and characteristics of the baroclinic waves, which may have also contributed to the difference in wave characteristics among the four experiments. We also did not make comparison of frequencies of gravity waves in experiments with varying Coriolis parameters (the β effect). We speculate the inclusion of the β effect is also likely to change the gravity wave characteristics through its modification of the baroclinic development. Although it is found that the frequencies of gravity waves tend to increase with the growth rate of the background baroclinic waves and flow imbalance, what may determine the temporal and spatial scales of the jet-exit-region gravity waves remains unclear. A recent study of Plougonven and Snyder (2005) applied the "wave capture" theory of Bühler and McIntyre (2005) to explain the mechanism of the scale selection. Future research will explore the applicability of this theory to the gravity waves examined in the current study.

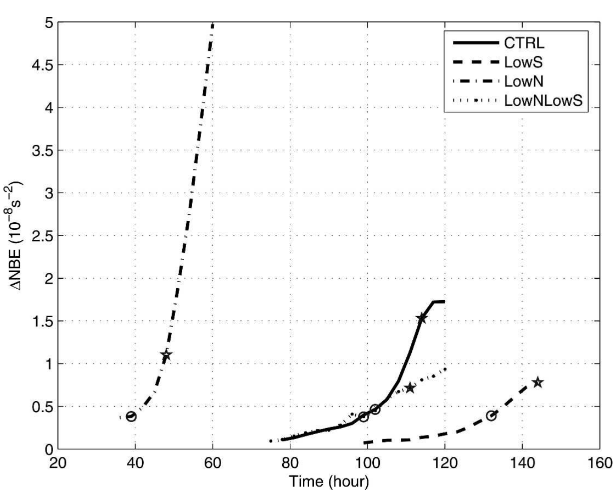

FIG. 17. Time evolution of ΔNBE (10^{-8} s^{-2}) averaged at the 10 points with the maximum values for the four experiments. The circles indicate the times for each case in Figs. 2–4 and 15–16. The stars indicate the times plotted in Figs. 5 and 7–13.

Acknowledgments. The authors benefited from discussions with Craig Epifanio, John Nielsen-Gammon, Chris Snyder, Riwal Plougonven, and Jason Sippel. This research was supported by National Science Foundation Grants ATM 0203238.

REFERENCES

Badger, J., and B. J. Hoskins, 2001: Simple initial value problems and mechanisms for baroclinic growth. *J. Atmos. Sci.,* **58,** 38–49.

Bosart, L. F., W. E. Bracken, and A. Seimon, 1998: A study of cyclone mesoscale structure with emphasis on a large-amplitude inertia-gravity waves. *Mon. Wea. Rev.,* **126,** 1497–1527.

Bühler, O., and M. E. McIntyre, 2005: Wave capture and wave-vortex duality. *J. Fluid Mech.,* **534,** 67–95.

Charney, J. G., 1955: The use of primitive equations of motion in numerical prediction. *Tellus,* **7,** 22–26.

Davis, C. A., and K. A. Emanuel, 1991: Potential vorticity diagnosis of cyclogenesis. *Mon. Wea. Rev.,* **119,** 1929–1952.

Dudhia, J., 1993: A nonhydrostatic version of the Penn State–NCAR Mesoscale Model: Validation tests and simulation of an Atlantic cyclone and cold front. *Mon. Wea. Rev.,* **121,** 1493–1513.

Fritts, D. C., and M. J. Alexander, 2003: Gravity wave dynamics and effects in the middle atmosphere. *Rev. Geophys.,* **41,** 1003–1063.

Guest, F. M., M. J. Reeder, C. J. Marks, and D. J. Karoly, 2000: Inertia gravity waves observed in the lower stratosphere over Macquarie Island. *J. Atmos. Sci.,* **57,** 737–752.

Hakim, G. J., 2000: Role of nonmodal growth and nonlinearity in cyclogenesis initial-value problem. *J. Atmos. Sci.,* **57,** 2951–2967.

Holton, J. R., P. H. Haynes, M. E. McIntyre, A. R. Douglass, R. B. Road, and L. Pfister, 1995: Stratosphere–troposphere exchange. *Rev. Geophys.,* **33,** 403–439.

Koch, S. E., and P. B. Dorian, 1988: A mesoscale gravity wave event observed over CCOPE. Part III: Wave environment and probable source mechanisms. *Mon. Wea. Rev.,* **116,** 2570–2592.

——, and C. O'Handley, 1997: Operational forecasting and detection of mesoscale gravity waves. *Wea. Forecasting,* **12,** 253–281.

——, F. Zhang, M. L. Kaplan, Y.-L. Lin, R. Weglarz, and M. Trexler, 2001: Numerical simulation of a gravity wave event observed during CCOPE. Part III: Mountain–plain solenoids in the generation of the second wave episode. *Mon. Wea. Rev.,* **129,** 909–932.

Koppel, L. L., L. F. Bosart, and D. Keyser, 2000: A 25-yr climatology of large-amplitude hourly surface pressure changes over the conterminous United States. *Mon. Wea. Rev.,* **128,** 51–68.

Lim, J. S., 1989: *Two-Dimensional Signal and Image Processing*. Prentice Hall, 880 pp.

Lindzen, R. S., and B. Farrell, 1980: A simple approximate result for the maximum growth rate of baroclinic instabilities. *J. Atmos. Sci.,* **37,** 1648–1654.

O'Sullivan, D., and T. J. Dunkerton, 1995: Generation of inertia-gravity waves in a simulated life cycle of baroclinic instability. *J. Atmos. Sci.,* **52,** 3695–3716.

Pierrehumbert, R. T., and K. L. Swanson, 1995: Baroclinic instability. *Annu. Rev. Fluid Mech.,* **27,** 419–467.

Plougonven, R., and H. Teitelbaum, 2003: Comparison of a large-scale inertia-gravity wave as seen in the ECMWF analyses and from radiosondes. *Geophys. Res. Lett.,* **30,** 1954–1957.

——, and C. Snyder, 2005: Gravity waves excited by jets: Propagation versus generation. *Geophys. Res. Lett.,* **32,** L18802, doi:10.1029/2005GL023730.

Ramamurthy, M. K., R. M. Rauber, B. P. Collins, and N. K. Malhotra, 1993: A comparative study of large-amplitude gravity-wave events. *Mon. Wea. Rev.,* **121,** 2951–2974.

Raymond, D. J., 1992: Nonlinear balance and potential-vorticity thinking at large Rossby number. *Quart. J. Roy. Meteor. Soc.,* **118,** 987–1015.

Rotunno, R., and J.-W. Bao, 1996: A case study of cyclogenesis using a model hierarchy. *Mon. Wea. Rev.,* **124,** 1051–1066.

——, W. C. Skamarock, and C. Snyder, 1994: An analysis of frontogenesis in numerical simulations of baroclinic waves. *J. Atmos. Sci.,* **51,** 3373–3398.

Salby, M. L., and R. R. Garcia, 1987: Transient response to localized episodic heating in the tropics. Part I: Excitation and short-time near-field behavior. *J. Atmos. Sci.,* **44,** 458–498.

Schneider, R. S., 1990: Large-amplitude mesoscale wave disturbances within the intense Midwest extratropical cyclone of 15 December 1987. *Wea. Forecasting,* **5,** 533–558.

Shapiro, M. A., 1981: Frontogenesis and geostrophically forced secondary circulations in the vicinity of jet stream–frontal zone systems. *J. Atmos. Sci.,* **38,** 954–973.

——, and D. Keyser, 1990: Fronts, jet streams, and the tropopause. *Extratropical Cyclones: The Erik Palmen Memorial Volume,* C. W. Newton and E. O. Holopainen, Eds., Amer. Meteor. Soc., 167–191.

Simmons, A. J., and B. J. Hoskins, 1978: The life cycles of some nonlinear baroclinic waves. *J. Atmos. Sci.,* **35,** 414–432.

Uccellini, L. W., and S. E. Koch, 1987: The synoptic setting and possible source mechanisms for mesoscale gravity wave events. *Mon. Wea. Rev.,* **115,** 721–729.

Wu, D. L., and F. Zhang, 2004: A study of mesoscale gravity waves over North Atlantic with satellite observations and a mesoscale model. *J. Geophys. Res.,* **109,** D22104, doi:10.1029/2004JD005090.

Zhang, F., 2004: Generation of mesoscale gravity waves in the upper-tropospheric jet front systems. *J. Atmos. Sci.,* **61,** 440–457.

——, and S. E. Koch, 2000: Numerical simulations of a gravity wave event over CCOPE. Part II: Waves generated by an orographic density current. *Mon. Wea. Rev.,* **128,** 2777–2796.

——, ——, and M. L. Kaplan, 2000: A survey of unbalanced flow diagnostics and their application. *Adv. Atmos. Sci.,* **17,** 165–173.

——, ——, C. A. Davis, and M. L. Kaplan, 2001: Wavelet analysis and the governing dynamics of a large-amplitude gravity wave event along the east coast of the United States. *Quart. J. Roy. Meteor. Soc.,* **127,** 2209–2245.